Anomalous Hall effect induced by Berry curvature in the topological nodal-line van der Waals ferromagnet Fe_4GeTe_2

Satyabrata Bera,[1,*] Sudipta Chatterjee,[2,*] Subhadip Pradhan,[3,*] Suman Kalyan Pradhan,[1] Sk Kalimuddin,[1] Arnab Bera,[1] Ashis K. Nandy,[3,†] and Mintu Mondal[1,‡]

[1]*School of Physical Sciences, Indian Association for the Cultivation of Science, Jadavpur, Kolkata 700032, India*

[2]*Department of Condensed Matter and Materials Physics, S. N. Bose National Centre for Basic Sciences, JD Block, Sector III, Salt Lake, Kolkata 700106, India*

[3]*School of Physical Sciences, National Institute of Science Education and Research Bhubaneswar, An OCC of Homi Bhabha National Institute, Khurda Road, Jatni, Odisha 752050, India*

(Received 20 March 2023; revised 26 July 2023; accepted 29 August 2023; published 12 September 2023)

The exploration of nontrivial transport phenomena associated with the interplay between magnetic order and spin-orbit coupling (SOC), particularly in van der Waals (vdW) systems, has gained a resurgence of interest due to their easy exfoliation, ideal for two-dimensional (2D) spintronics. We report the near room temperature quasi-2D ferromagnet, Fe_4GeTe_2 from the iron-based vdW family (Fe_nGeTe_2, $n = 3,4,5$), exhibiting a large anomalous Hall conductivity (AHC), $\sigma^A_{xy} \sim 490\,\Omega^{-1}\text{cm}^{-1}$ at 2 K. The near quadratic behavior of anomalous Hall resistivity (ρ^A_{xy}) with the longitudinal resistivity (ρ_{xx}) suggests that a dominant AHC contribution is coming from an intrinsic Berry curvature (BC) mechanism. Concomitantly, the electronic structure calculations reveal a large BC arising from SOC induced gapped nodal lines around the Fermi level, governing such large AHC property. Moreover, we also report an exceptionally large anomalous Hall angle ($\simeq$10.6%) and Hall factor ($\simeq$0.22 V^{-1}) values which, so far, are the largest in compared to those for other members in this vdW family.

DOI: 10.1103/PhysRevB.108.115122

I. INTRODUCTION

Topological semimetals (TSMs) are characterized by gapless low-energy electronic states that can be protected by symmetries and simultaneously, offer an excellent platform for exploring unconventional transport phenomena [1–5]. By examining the electronic structures, the TSMs can be further classified into Dirac semimetals (DSMs), Weyl semimetals (WSMs), and nodal-line semimetals (NLSMs) depending on the degeneracy and dimensions of the band crossings in the Brillouin zone (BZ). The DSMs [6–11] with fourfold degenerate band crossing point may transform into twofold degenerate WSMs [12–15] carrying chiral charges which are attributed to certain symmetry breaking. In the case of NLSMs, the band crossings either form a closed loop or a line instead of discrete points in the BZ [16–22].

Recently, various magnetic systems carrying topologically nontrivial quantum states protected by symmetries governed by their magnetic order, have attracted tremendous attention, owing to the unusual transport properties like anomalous Hall effect (AHE) [15,20–24], anomalous Nernst effect, etc. [25,26]. In particular, the AHE becomes one of the most intriguing transport phenomena in magnetic TSMs in which transverse charge current is generated without any external magnetic fields. Especially, the intrinsic contribution to AHE comes from the topologically nontrivial states via a geometrical quantity in the band structures—the Berry curvature (BC) [27]. A gapless nodal line often does not exhibit a net BC and hence, the anomalous Hall conductivity (AHC) calculated for such nodal-line features near about the Fermi energy (E_F) turns out to be zero. These topological features are generally protected by mirror symmetry [28,29], which may break in the presence of spin-orbit coupling (SOC) in magnetic systems [30,31], then the nodal line gets either gapped out fully or evolves into a pair of Weyl points [32]. In both cases, the AHC can be observed and tuned by changing the electronic structures through suitable manipulation of the magnetic state [15,32–34].

The class of quasi-two-dimensional (2D) van der Waals ferromagnet (vdW-FM) provides an excellent platform for investigating many of these novel topological transport phenomena in the 2D limit by probing AHE. However, in most cases, the 2D vdW-FMs such as Cr(Si, Ge)Te_3 [35], CrI_3 [36], etc., show magnetic transition temperatures (T_c) well below the room temperature, making them unsuitable for 2D spintronic applications. Very recently, there has been renewed interest in Fe-based 2D vdW-FMs where the T_c can be increased with the Fe concentration, by means of increasing n from three to five in the Fe_nGeTe_2 (FnGT) vdW family [37–42]. With increasing n, the Fe-rich slab making the bulk system exhibits increased strength in exchange interactions between Fe moments, and hence, the T_c of the corresponding member increases [41]. Additionally, their physical properties significantly differed based on the value of n due to the changes in their electronic structures [20,37,43–47]. As

*These authors contributed equally to this work.
†aknandy@niser.ac.in
‡sspmm4@iacs.res.in

an example, the $n = 3$ member having the closest stoichiometric Fe concentration ($Fe_{2.91}GeTe_2$, $T_c \simeq 220$ K) shows moderately large anomalous Hall angle (Θ_{AH}) and Hall factor (S_H), which are ≈9% and 0.17 V^{-1}, respectively [20]. Note, in this vdW-FM family, the only nonzero AHC component is σ^A_{xy} [45]. The experimentally reported σ^A_{xy} for Fe_3GeTe_2 (F3GT) is ≈540 $\Omega^{-1}cm^{-1}$, much larger than the theoretically measured value, ≈180 $\Omega^{-1}cm^{-1}$ [20]. The above room temperature candidate, Fe_5GeTe_2 (F5GT), however, shows the maximum AHC value about 120 $\Omega^{-1}cm^{-1}$ near temperatures of about 100 K [40]. In particular, the theoretically designed F4GT sample by Seo *et al*. [41] has gained tremendous attention when experimentally it was found as a good candidate showing large magnetization and high conductivity near room temperatures ($T_c \simeq 270$ K) and these properties were well retained even when it is cleaved.

In this study, we investigate the topological aspects of AHE for the Fe_4GeTe_2 (F4GT) sample which is found to show a large AHC value, ∼490 $\Omega^{-1}cm^{-1}$ at 2 K, comparable with the F3GT sample. Although, a few theoretical works have been primarily focused on comparing anomalous transport properties among F*n*GT members [45,48], a well-connected experimental and theoretical study to understand transport properties in F4GT is still lacking. Experimentally, based on the Kaplus-Luttinger (KL) mechanism, we have identified that in F4GT the most contribution to AHC is coming from intrinsic BCs, and the estimated value is ≈462 $\Omega^{-1}cm^{-1}$. This has been further confirmed by electronic structure calculations where the theoretically estimated value is about 485 $\Omega^{-1}cm^{-1}$ at E_F. We find that such a large AHC results from BC induced by the gapped nodal line near about E_F in the presence of SOC. Furthermore, in our sample, exceptionally large Θ_{AH} (≈10.6%) and S_H (≈0.22 V^{-1}) values are simultaneously observed.

II. METHODS

High-quality single crystals of F4GT were grown by the chemical vapor transport (CVT) method using I_2 as a transport agent (see Sec. S1(A) of the Supplemental Material [49]). The crystal structures of F4GT (both primitive and conventional unit cell) are depicted in Fig. 1(a), and the x-ray diffraction (XRD) pattern of the F4GT single crystal at room temperature is given in Fig. S2 in the Supplemental Material (SM) [49]. The crystal morphology and chemical compositions of the samples were analyzed using a high-vacuum scanning electron microscope (SEM), specifically the JEOL LSM-6500 model. Results are discussed in Sec. S1(C) of the Supplemental Material [49].

The magnetization measurements of the sample were performed using a magnetic property measurement system (MPMS-SQUID, Quantum Design, USA). The magnetization data up to an applied field of 5 T and temperature down to 2 K were recorded. The sample used for the magnetic measurements was of approximate dimensions 1.4 × 1.4 × 0.06 mm^3. The electrical and magnetic transport measurements were carried out by using a 9 T Physical Property Measurement System (PPMS, Quantum Design, USA) using the electrical transport option (ETO). Measurements of both longitudinal (ρ_{xx}) and Hall (ρ_{xy}) resistivities were done in a

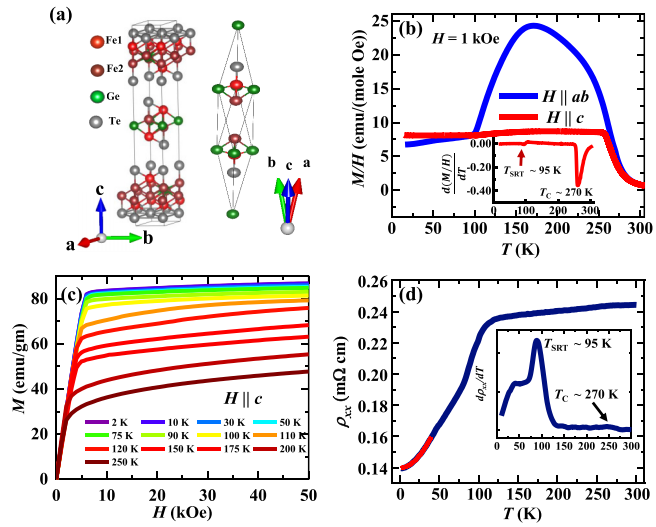

FIG. 1. (a) The crystal structures of F4GT are represented in the conventional (hexagonal) and primitive (rhombohedral) unit cells. (b) Temperature dependence of dc magnetization measured in the zero-field-cooled condition for applied magnetic field $H = 1\,kOe$ with $H \parallel ab$ and $H \parallel c$, respectively. Inset shows the derivative of M, i.e., $(\frac{d(M/H)}{dT})$ vs T plot. (c) The M variation as a function of an applied magnetic field along c axis at different Ts. (d) Temperature dependence zero field electrical resistivity curve with current through in-plane direction ($I \parallel ab$ plane). The solid red line shows the fit of $\rho_{xx} \propto T^2$. Inset shows the temperature derivative of ρ_{xx}.

standard four-probe method using conducting silver paint and gold wires. The current ($I = 100\,\mu A$) is applied along the ab plane and the applied magnetic field along the c axis of the sample. In order to effectively eliminate the ρ_{xx} contribution coming from the voltage probe misalignment, the final ρ_{xy} is obtained by the difference of transverse resistivity measured at the positive and negative magnetic fields.

III. RESULTS AND DISCUSSION

A. Magnetization and resistivity

Figure 1(b) shows the temperature-dependent dc magnetization (M) under 1 kOe applied magnetic field in parallel to the ab and c directions of the F4GT single crystal. A sharp increase in M is observed with decreasing temperature, which clearly signifies a paramagnetic (PM) to an FM phase transition. The observed magnetic behavior of F4GT is consistent with previous reports [40,50]. From the $\frac{d(M/H)}{dT}$ vs T curve shown in the inset of Fig. 1(b), the estimated T_c (Curie temperature) is about 270 K. With further lowering the temperature, the magnetic moment along the ab plane continuously increases to maxima, then quickly decreases and becomes equivalent to the moment along the c axis. In the temperature range 270–160 K, the majority of Fe atoms at sites other than Fe1 (i.e., Fe2) and minor proportions of Fe1 align along the direction of the field. Therefore, the resultant moment of the system is ferromagnetically ordered. Below 160 K down to 100 K, a major proportion of the Fe atoms at Fe1 sites, initially, in a disordered state, reorients and interact with the other Fe atoms. This reduces the magnetic

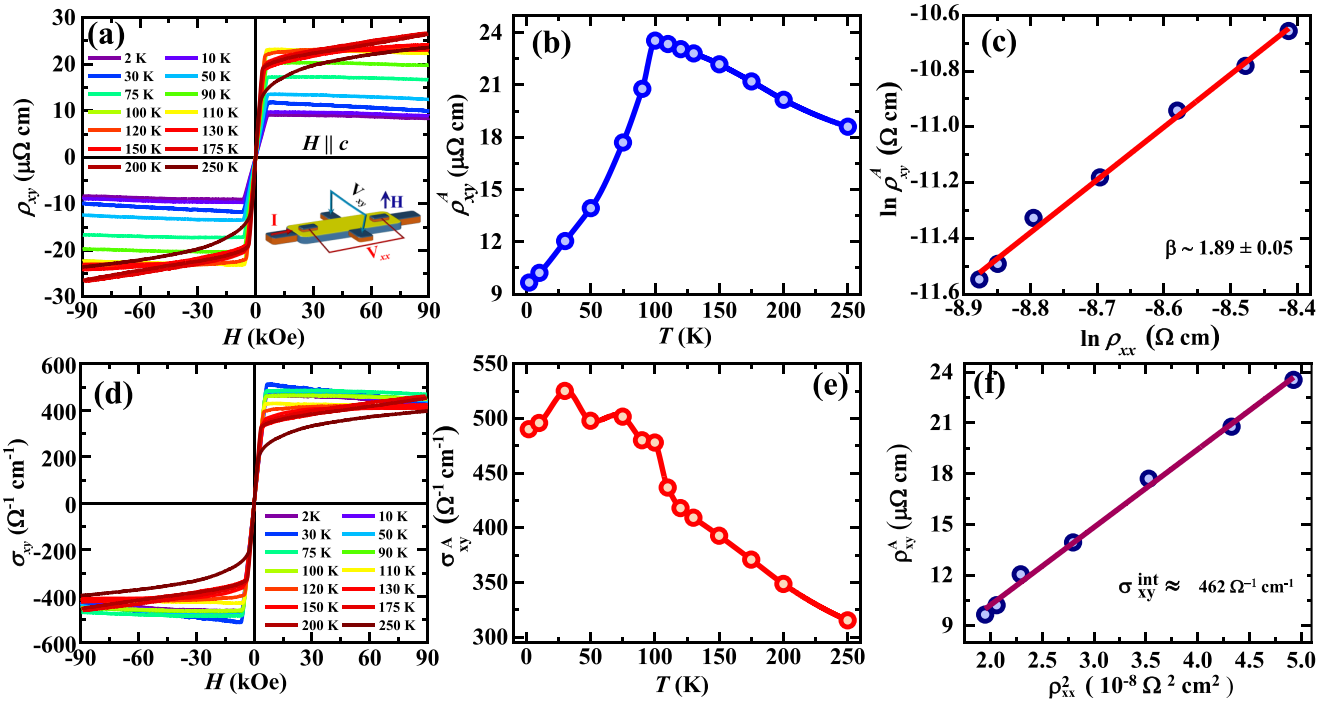

FIG. 2. (a) Magnetic field dependent Hall resistivity (ρ_{xy}) at various temperatures ranging from 2 K to 250 K. Inset: The schematic diagram of the sample device used for longitudinal voltage V_{xx} and the Hall voltage V_{xy} measurements. (b) Temperature dependence of anomalous Hall resistivity ρ^A_{xy}. (c) The plot of $\ln\rho^A_{xy}$(T) vs $\ln\rho_{xx}$(T), with the solid red line representing the fit using the relation $\rho^A_{xy} \propto \rho^\beta_{xx}$. (d) Field-dependent Hall conductivity (σ_{xy}) at various indicated temperatures. (e) Temperature-dependent anomalous Hall conductivity (σ^A_{xy}). (f) Plot between ρ^A_{xy} and ρ^2_{xx}, and the fitting using Eq. (3) is shown in solid line.

moment with decreasing temperature [50]. By further decreasing temperature, another magnetic transition is observed at $T \approx 95$ K, matching well with the recently reported spin-reorientation transition temperatures (T_{SRT}) [40,41]. Below T_{SRT}, the moment value along the c axis is a little larger than ab plane which signifies the switching of the easy axis of the magnetization. The above results reveal the reorientation of the magnetic easy axis towards the c direction from the ab plane below T_{SRT} [50].

In Fig. 1(c), the isothermal magnetization as a function of an applied magnetic field for different temperatures is shown up to 5 T along the c direction. The M-H data along the ab direction is incorporated in the Supplemental Material (see Fig. S4) [49]. At temperatures well below T_c, each $M(H)$ isotherm shows a sharp increase in the low field region and a saturationlike behavior in the high field region. The saturation magnetization decreases continuously as the temperature increases, and the overall nature of the $M(H)$ isotherms changes significantly as we approach T_c. The temperature-dependent ρ_{xx} is shown in Fig. 1(d) where the residual resistivity value is ~ 0.1396 mΩ cm at 2 K, yielding a residual resistivity ratio [RRR $= \rho_{xx}(300\,\text{K})/\rho_{xx}(2\,\text{K})$] of ~ 1.75. The $d\rho_{xx}/dT$ vs T plot in the inset of Fig. 1(d) further reveals clear slope changes near $T_{SRT} \sim 95$ K and $T_c \sim 270$ K which strongly supports the magnetic origin of phase transitions around the T_{SRT} and T_c. A clear anomaly in the resistivity data is observed around 40 K. This anomaly is related to the Fermi-liquid behavior of the present compound where the ρ_{xx} shows a quadratic temperature dependence [51]. To establish the Fermi liquid behavior for the present compound, the resistivity data is fitted from 2 K to 40 K using $\rho_{xx} \propto T^2$. The observed temperature behavior of transport properties is consistent with the previous report [41].

B. Anomalous Hall effect

We have now carried out detailed magnetotransport measurements over a wide range of temperatures to study the AHE in this compound. Figure 2(a) depicts the Hall resistivity (ρ_{xy}) as a function of the applied magnetic field for temperatures ranging from 2 K to 250 K. The $\rho_{xy}(H)$ grows sharply for a small applied magnetic field and anomalous behavior is observed up to ~ 0.6 T. In the high field region, $\rho_{xy}(H)$ shows a weak linear field dependence up to a magnetic field of 9 T. Similarities in the forms of the $M(H)$ and $\rho_{xy}(H)$ curves clearly indicate the presence of AHE in the investigated studied compound. As we approach the T_c, the overall character of the $\rho_{xy}(H)$ curves changes substantially in both the low field and the high field regions. Generally, in addition to the ordinary Hall effect, ρ_{xy} in a FM material has an additional contribution from M and is expressed as

$$\rho_{xy}(H) = \rho^0_{xy} + \rho^A_{xy} = R_0 \mathrm{H} + R_s \mu_0 M, \tag{1}$$

where ρ^0_{xy} and ρ^A_{xy} are the ordinary and anomalous contributions to the Hall resistivity, with R_0 and R_s being the normal and anomalous Hall coefficients, respectively. The values of R_0 and ρ^A_{xy} are determined from the linear fit to the $\rho_{xy}(H)$ curve in the high field region, where the slope and the y-axis intercept of the linear fit correspond to R_0 and ρ^A_{xy}, respectively. Figure 2(b) depicts the variation of the ρ^A_{xy} as a function

of temperature, demonstrating that the ρ_{xy}^{A} increases with rising temperature from 2 K to approximately 100 K, and then starts decreasing above 100 K.

To elucidate the mechanism responsible for the observed AHE in F4GT, we have plotted ρ_{xy}^{A} vs ρ_{xx} on a double logarithm scale, and a fitting was employed to evaluate the exponent β using the relation $\rho_{xy}^{A} \propto \rho_{xx}^{\beta}$ [27], as shown in Fig. 2(c). As above ∼100 K, the magnetic transition comes into play and ρ_{xy}^{A} starts decreasing at higher temperatures. So, for a good comparison, the plot between ρ_{xy}^{A} and ρ_{xx} is restricted in the temperature range from 2 K to 100 K, and this has been addressed previously for several metallic ferromagnets [24,52,53]. The near-quadratic relationship between ρ_{xy}^{A} and ρ_{xx} (i.e., $\beta \approx 2$) strongly indicates that the intrinsic KL or the extrinsic side-jump mechanism dominates in the AHE rather than the extrinsic skew-scattering mechanism. Furthermore, we have also calculated the Hall conductivity (σ_{xy}) using the tensor conversion relation [24] as

$$\sigma_{xy} = \frac{\rho_{xy}}{\left(\rho_{xx}^{2} + \rho_{xy}^{2}\right)}. \tag{2}$$

Figure 2(d) demonstrates the field dependence of Hall conductivity at various temperatures. The AHC is obtained by extrapolating the high-field σ_{xy} data to zero fields on the y axis. The temperature dependence of AHC is shown in Fig. 2(e). At 2 K, a large value of AHC is observed to be $\sim 490\,\Omega^{-1}\mathrm{cm}^{-1}$. The temperature-dependent AHC and ρ_{xy}^{A} are presented in Fig. S5 of the Supplemental Material [49], and the change of AHC is almost temperature independent, showing that the origin of AHE in F4GT is intrinsic in nature [53]. To extract the intrinsic AHC value, we have fitted ρ_{xy}^{A} vs ρ_{xx}^{2} plot as illustrated in Fig. 2(f), using the following equation [24,53]:

$$\rho_{xy}^{A} = f(\rho_{xx0}) + \sigma_{xy}^{\mathrm{int}} \rho_{xx}^{2}, \tag{3}$$

where the first term, i.e., $f(\rho_{xx0})$, is a function of residual resistivity ρ_{xx0}, which includes the contributions due to skew scattering as well as side-jump mechanisms, and $\sigma_{xy}^{\mathrm{int}}$ is the AHC purely due to the intrinsic Berry curvature mechanism [24,53]. The estimated $\sigma_{xy}^{\mathrm{int}}$ is found to be about $462\,\Omega^{-1}\mathrm{cm}^{-1}$. As a result, the intrinsic Berry phase-driven mechanism is responsible for more than 90% of the total AHC. The extrinsic side-jump contribution of AHC $|\sigma_{xy,sj}^{A}|$ has been shown to be in the order of $(e^{2}/(ha)(\epsilon_{\mathrm{SOC}}/E_{F}))$, where ϵ_{SOC} is the SOC strength [54,55]. For metallic FMs, $(\epsilon_{\mathrm{SOC}}/E_{\mathrm{F}})$ is usually in the order of 10^{-2} [52,53]. Consequently, the extrinsic side-jump contribution to AHC should be very small or negligible in comparison to the intrinsic AHC. Therefore, the AHE in F4GT is primarily dominated by the intrinsic Berry phase-driven KL mechanism. Theoretically, the intrinsic AHC is of the order of $e^{2}/(ha)$ in the resonance condition, where e is the electronic charge, h is Planck's constant, and a is the lattice constant [55,56]. Taking $a = \mathrm{V}^{1/3} \sim 7.32$ Å for the studied compound [57], we estimate the intrinsic AHC to be around $\sim 525\,\Omega^{-1}\mathrm{cm}^{-1}$ for F4GT, which is closer to our experimentally observed value of $462\,\Omega^{-1}\mathrm{cm}^{-1}$ [58].

To further assess the strength of AHE in such vdW FM, we have estimated the two characteristic quantities, namely the anomalous Hall angle, Θ_{AH} and the anomalous Hall factor, S_{H}. The former can be determined as, $\Theta_{\mathrm{AH}} = \sigma_{xy}^{A}/\sigma_{xx}$,

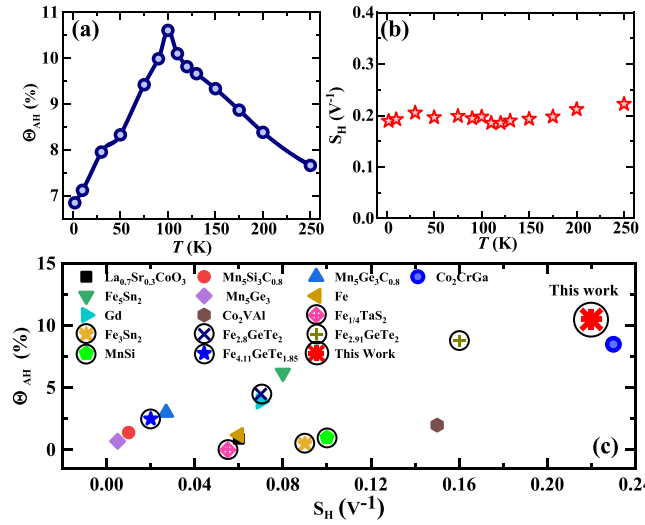

FIG. 3. (a) and (b) represent the Θ_{AH} and the S_{H} as a function of temperature, respectively. (c) The Θ_{AH} and S_{H} of the F4GT compound are plotted along with the other previously reported metallic FMs. Particularly, the symbols enclosed by the black empty circle represent vdW materials.

measuring the strength of the transverse current generated with respect to the applied normal current [27]. The latter one is defined as, $S_{\mathrm{H}} = \sigma_{xy}^{A}/M$, the measure of sensitivity of AHC with respect to M [59]. Figures 3(a) and 3(b) show the plot of Θ_{AH} and S_{H} as function of temperature, respectively. The Θ_{AH} value reaches maximum which is about 10.6% at $\mathrm{T_{SRT}}$ and it is also significantly large (∼7.6%) even at $T = 250$ K. On the other hand, the S_{H} remains almost invariant with T, and a maximum value of about 0.22 V^{-1} is obtained at 250 K. Such surprising coexistence of large Θ_{AH} and S_{H} within a wide temperature window has led us to compare those quantities with other known metallic FMs, as shown in Fig. 3(c). It is extremely rare to find a ferromagnetic metallic system with both large Θ_{AH} and S_{H} [20]. From Fig. 3(c), we infer that the F4GT shows significantly larger Θ_{AH} and S_{H} values compared to all previously reported metallic ferromagnets [53,57,59–63].

C. First-principles calculations

In order to investigate the intrinsic origin of AHE for F4GT, we performed first-principles electronic structure calculations within density functional theory (DFT) formalism where the band structure is further parametrized using maximally localized Wannier functions (ML-WFs) for AHC calculations. Details of the computational methodology and numerical AHC simulations are provided in the SM [49]. All calculations are performed using the primitive rhombohedral unit cell and the band strictures are plotted along the lines connecting high symmetry points in the BZ, as shown in Fig. S6. Within magnetic calculations, the spin-resolved atom projected density of states in Fig. S6(c) from SM [49] clearly indicate two types of Fe atoms having the magnetic moments, 1.94 and 2.64 μ_B for Fe1 and Fe2, respectively. The average

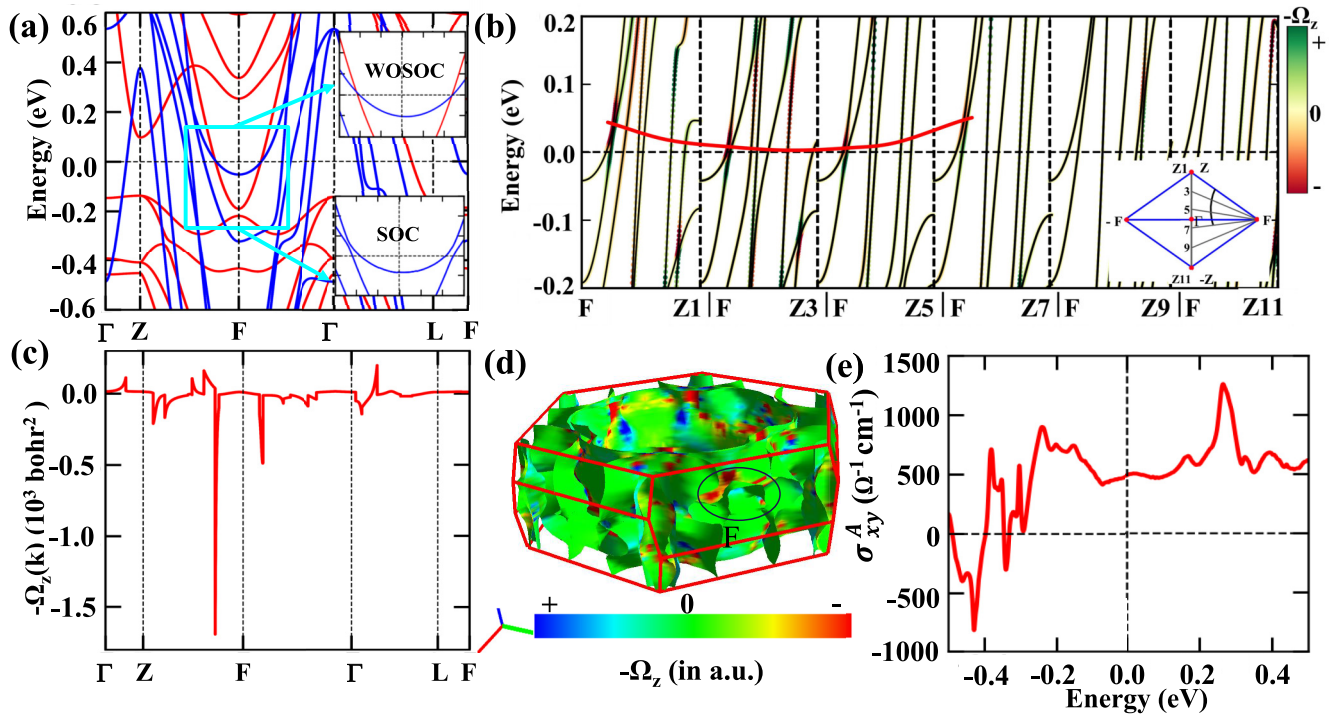

FIG. 4. (a) F4GT band structure is calculated for the primitive rhombohedral unit cell [Fig. 1(a)] without SOC for the majority (blue) and minority (red) spin channels. In the inset, the zoomed band structures around the high-symmetric F point in the BZ show the gap opening with SOC. (b) The BC induced by SOC for various k-path segments (the inset) is shown along the gapped nodal line where the red curved line passing through all blue boxes is the guide to the eye. The color bar represents the amplitude of the Ω_Z. (c) The BC plot along the high-symmetry path in the BZ for $E = E_F$. (d) The 3D map of Ω_Z in the full BZ shows the hot spots (e.g., like the closed black circle) around F point with a large BC value. (e) σ^A_{xy} is calculated from BCs over full BZ within the energy range -0.5 eV to 0.5 eV around E_F.

magnetic moment per Fe atom is slightly higher than the experimentally reported value ($\sim 2.12\,\mu_B$/Fe) [50].

By analyzing the band structure without SOC, we identify two band crossing points along FZ and $F\Gamma$ directions in the close vicinity of E_F, see the boxed region in Fig 4(a). Two inset figures describe that by introducing SOC in our calculations, the crossing points are gapped out. In order to identify the nodal line, we have calculated band structures without SOC along several line segments connecting the F point and a few points on the $\bar{Z}\Gamma Z$ line, see Fig. S8 of the SM [49]. Near E_F, the nodal line is depicted by joining the crossing points of bands (up and down) by a curved black line, i.e., a dispersive gapless nodal line. The projected orbital analysis, see Fig. S7 in the SM [49], suggests that those key bands have strong hybridization primarily between Fe-d (d_{yz}, d_{xz}, and d_{z^2}) and Te-p (p_y) orbitals. The twofold degeneracy of the nodal line is lifted with the inclusion of SOC. Therefore, the gapped nodal line in the presence of SOC is found to generate nonzero BC, see Fig. 4(b) as well as Fig. S9 in the SM [49]. It is evident from Fig. S9(b) of the SM [49] that a strong BC is generated by the SOC-induced gap between bands at E_F. Moreover, the color map denoting the BC contributions on band structures for various line segments, see the inset of Fig. 4(b), infers that the gapped nodal line in the $FZ\Gamma$ plane plays the key role in generating the BC in F4GT. In Fig. 4(c), the calculated BC at slightly above E_F as a function of momentum k along the high symmetric directions also reveals a large value around the F point, and the largest value is found along the FZ direction. The three-dimensional Fermi surface plot in conjunction with the BC color map in Fig. 4(d) further strengthens these observations by identifying hot spots (e.g., like the black, circled one) near the F point region point. This also yields that the major contributor to the BC in the BZ comes from those hot spots. After identifying the BC contribution from band structure, we have performed the numerical calculations for AHC (see Sec. S4 of the SM for details [49]). Note, the calculated AHC shown in Fig. 4(e) will be completely intrinsic. We observe a nearly constant value within a range of 100 meV around E_F and the calculated value is about 485 Ω^{-1}cm^{-1} at E_F. This is now attributed to the BC arising from the gapped nodal line and the value is in close agreement with the experimentally estimated intrinsic AHC value ($\sim 462\,\Omega^{-1}$cm^{-1}). It is also noteworthy that we observe a significant change in transport properties above the T_{SRT}, as demonstrated in Figs. 1(d) and 2(b). Additionally, we have explored from the first-principle electronic structure calculations that the AHC is changing gradually with a change in magnetization orientation (see Sec. S5(E) of the Supplemental Material [49]). This is due to the change in BC obtained from the calculated band structure.

IV. CONCLUSIONS

In summary, we have systematically investigated the AHE in a quasi-2D vdW FM, Fe_4GeTe_2, a member in the Fe_nGeTe_2 family. The detailed analysis of our results reveals

that F4GT exhibits a significantly large AHE along with a rare coexistence of a large anomalous Hall angle, $\Theta_{AH} \simeq 10.6\%$, and a large anomalous Hall factor, $S_H \simeq 0.22\ V^{-1}$. The ρ_{xy}^A scales near quadratically with ρ_{xx}, and our comprehensive experimental analysis reveals that the observed large AHE in the F4GT compound is attributed to an intrinsic BC-driven KL mechanism. Experimentally, a large AHC $\sigma_{xy} \sim 500\,\Omega^{-1}\text{cm}^{-1}$ with an intrinsic contribution of $\sim 462\,\Omega^{-1}\text{cm}^{-1}$ is seen at 2 K. Theoretically, our band structure calculations establish that such a large BC is owing to the gapped nodal line in the presence of SOC. Notably, our first-principles calculation also predicts an intrinsic AHC value of 485 $\Omega^{-1}\text{cm}^{-1}$, which is in good agreement with the aforementioned experimentally observed value. Therefore, the coexistence of exceptionally large AHC, Θ_{AH}, and S_{H} values along with a better T_c, make F4GT a suitable candidate for 2D spintronic devices in comparison to other vdW FMs.

Note added. We are also aware of the experimental work on the recent arXiv paper [51] dealing with, primarily, magnetoresistance and briefly on AHE in the same system but on the F4GT flake instead of a bulk single crystal presented here.

ACKNOWLEDGMENTS

This work was supported by the Department of Science and Technology (DST), Government of India (Grants No. SRG/2019/000674 and No. EMR/2016/005437), S.B. and A.B. thank CSIR Government of India for Research Fellowship with Grants No. 09/080(1110)/2019-EMR-I and No. 09/080(1109)/2019-EMR-I, respectively. S.C. thanks Dr. B Ghosh and A. Panda for their help. S.P. and A.K.N. acknowledge the computational resources, Kalinga cluster, at the National Institute of Science Education and Research, Bhubaneswar, India. A.K.N. and S.P. thank Prof. P.M. Oppeneer for the Swedish National Infrastructure for Computing (SNIC) facility. The authors also thank the DST, India for the financial support during the experiments at the Indian Beamline, PF-18B, KEK, Japan, and Proposal No. 2021-IB-28

[1] X. Wan, A. M. Turner, A. Vishwanath, and S. Y. Savrasov, Topological semimetal and fermi-arc surface states in the electronic structure of pyrochlore iridates, Phys. Rev. B **83**, 205101 (2011).

[2] G. Xu, H. Weng, Z. Wang, X. Dai, and Z. Fang, Chern Semimetal and the Quantized Anomalous Hall Effect in $HgCr_2Se_4$, Phys. Rev. Lett. **107**, 186806 (2011).

[3] C.-K. Chiu, J. C. Y. Teo, A. P. Schnyder, and S. Ryu, Classification of topological quantum matter with symmetries, Rev. Mod. Phys. **88**, 035005 (2016).

[4] N. P. Armitage, E. J. Mele, and A. Vishwanath, Weyl and dirac semimetals in three-dimensional solids, Rev. Mod. Phys. **90**, 015001 (2018).

[5] B. Q. Lv, T. Qian, and H. Ding, Experimental perspective on three-dimensional topological semimetals, Rev. Mod. Phys. **93**, 025002 (2021).

[6] Z. Wang, Y. Sun, X.-Q. Chen, C. Franchini, G. Xu, H. Weng, X. Dai, and Z. Fang, Dirac semimetal and topological phase transitions in A_3Bi (A = Na, K, Rb), Phys. Rev. B **85**, 195320 (2012).

[7] L. P. He, X. C. Hong, J. K. Dong, J. Pan, Z. Zhang, J. Zhang, and S. Y. Li, Quantum Transport Evidence for the Three-Dimensional Dirac Semimetal Phase in Cd_3As_2, Phys. Rev. Lett. **113**, 246402 (2014).

[8] M. Neupane, S.-Y. Xu, R. Sankar, N. Alidoust, G. Bian, C. Liu, I. Belopolski, T.-R. Chang, H.-T. Jeng, H. Lin, A. Bansil, F. Chou, and M. Z. Hasan, Observation of a three-dimensional topological dirac semimetal phase in high-mobility Cd_3As_2, Nat. Commun. **5**, 3786 (2014).

[9] Z. K. Liu, B. Zhou, Y. Zhang, Z. J. Wang, H. M. Weng, D. Prabhakaran, S.-K. Mo, Z. X. Shen, Z. Fang, X. Dai, Z. Hussain, and Y. L. Chen, Discovery of a three-dimensional topological dirac semimetal, Na_3Bi, Science **343**, 864 (2014).

[10] M. M. Hosen, K. Dimitri, A. K. Nandy, A. Aperis, R. Sankar, G. Dhakal, P. Maldonado, F. Kabir, C. Sims, F. Chou, D. Kaczorowski, T. Durakiewicz, P. M. Oppeneer, and M. Neupane, Distinct multiple fermionic states in a single topological metal, Nat. Commun. **9**, 3002 (2018).

[11] G. Dhakal, F. Kabir, A. K. Nandy, A. Aperis, A. P. Sakhya, S. Pradhan, K. Dimitri, C. Sims, S. Regmi, M. M. Hosen, Y. Liu, L. Persaud, D. Kaczorowski, P. M. Oppeneer, and M. Neupane, Observation of anisotropic dirac cones in the topological material Ti_2Te_2P, Phys. Rev. B **106**, 125124 (2022).

[12] H. Weng, C. Fang, Z. Fang, B. A. Bernevig, and X. Dai, Weyl Semimetal Phase in Noncentrosymmetric Transition-Metal Monophosphides, Phys. Rev. X **5**, 011029 (2015).

[13] B. Q. Lv, H. M. Weng, B. B. Fu, X. P. Wang, H. Miao, J. Ma, P. Richard, X. C. Huang, L. X. Zhao, G. F. Chen, Z. Fang, X. Dai, T. Qian, and H. Ding, Experimental Discovery of Weyl Semimetal TaAs, Phys. Rev. X **5**, 031013 (2015).

[14] S.-Y. Xu, I. Belopolski, D. S. Sanchez, C. Zhang, G. Chang, C. Guo, G. Bian, Z. Yuan, H. Lu, T.-R. Chang *et al.*, Experimental discovery of a topological Weyl semimetal state in TaP, Sci. Adv. **1**, e1501092 (2015).

[15] P. Li, J. Koo, W. Ning, J. Li, L. Miao, L. Min, Y. Zhu, Y. Wang, N. Alem, C.-X. Liu *et al.*, Giant room temperature anomalous Hall effect and tunable topology in a ferromagnetic topological semimetal Co_2MnAl, Nat. Commun. **11**, 3476 (2020).

[16] A. A. Burkov, M. D. Hook, and L. Balents, Topological nodal semimetals, Phys. Rev. B **84**, 235126 (2011).

[17] C. Fang, Y. Chen, H.-Y. Kee, and L. Fu, Topological nodal line semimetals with and without spin-orbital coupling, Phys. Rev. B **92**, 081201(R) (2015).

[18] Y.-H. Chan, C.-K. Chiu, M. Y. Chou, and A. P. Schnyder, Ca_3P_2 and other topological semimetals with line nodes and drumhead surface states, Phys. Rev. B **93**, 205132 (2016).

[19] Q.-F. Liang, J. Zhou, R. Yu, Z. Wang, and H. Weng, Node-surface and node-line fermions from nonsymmorphic lattice symmetries, Phys. Rev. B **93**, 085427 (2016).

[20] K. Kim, J. Seo, E. Lee, K.-T. Ko, B. Kim, B. G. Jang, J. M. Ok, J. Lee, Y. J. Jo, W. Kang *et al.*, Large anomalous Hall current induced by topological nodal lines in a ferromagnetic van der waals semimetal, Nat. Mater. **17**, 794 (2018).

[21] S. Singh, J. Noky, S. Bhattacharya, P. Vir, Y. Sun, N. Kumar, C. Felser, and C. Shekhar, Anisotropic nodal-line-derived large anomalous Hall conductivity in ZrMnP and HfMnP, Adv. Mater. **33**, 2104126 (2021).

[22] S. N. Guin, Q. Xu, N. Kumar, H.-H. Kung, S. Dufresne, C. Le, P. Vir, M. Michiardi, T. Pedersen, S. Gorovikov *et al.*, 2d-berry-curvature-driven large anomalous Hall effect in layered topological nodal-line MnAlGe, Adv. Mater. **33**, 2006301 (2021).

[23] E. Liu, Y. Sun, K. Kumar, L. Muechler, A. Sun, L. Jiao, S-Y. Yang *et al.*, Giant anomalous Hall effect in a ferromagnetic kagome-lattice semimetal, Nat. Phys. **14**, 1125 (2018).

[24] K. Manna, L. Muechler, T.-H. Kao, R. Stinshoff, Y. Zhang, J. Gooth, N. Kumar, G. Kreiner, K. Koepernik, R. Car *et al.*, From Colossal to Zero: Controlling the Anomalous Hall Effect in Magnetic Heusler Compounds via Berry Curvature Design, Phys. Rev. X **8**, 041045 (2018).

[25] A. Sakai, Y. P. Mizuta, A. A. Nugroho, R. Sihombing, T. Koretsune, M.-T. Suzuki, N. Takemori, R. Ishii, D. Nishio-Hamane, R. Arita *et al.*, Giant anomalous nernst effect and quantum-critical scaling in a ferromagnetic semimetal, Nat. Phys. **14**, 1119 (2018).

[26] J. Xu, W. A. Phelan, and C.-L. Chien, Large anomalous nernst effect in a van der Waals ferromagnet Fe_3GeTe_2, Nano Lett. **19**, 8250 (2019).

[27] N. Nagaosa, J. Sinova, S. Onoda, A. H. MacDonald, and N. P. Ong, Anomalous Hall effect, Rev. Mod. Phys. **82**, 1539 (2010).

[28] L. Fu, Topological Crystalline Insulators, Phys. Rev. Lett. **106**, 106802 (2011).

[29] T. H. Hsieh, H. Lin, J. Liu, W. Duan, A. Bansil, and L. Fu, Topological crystalline insulators in the snte material class, Nat. Commun. **3**, 982 (2012).

[30] Q. Wang, Y. Xu, R. Lou, Z. Liu, M. Li, Y. Huang, D. Shen, H. Weng, S. Wang, and H. Lei, Large intrinsic anomalous Hall effect in half-metallic ferromagnet $Co_3Sn_2S_2$ with magnetic Weyl fermions, Nat. Commun. **9**, 3681 (2018).

[31] Z. Fang, N. Nagaosa, K. S. Takahashi, A. Asamitsu, R. Mathieu, T. Ogasawara, H. Yamada, M. Kawasaki, Y. Tokura, and K. Terakura, The anomalous Hall effect and magnetic monopoles in momentum space, Science **302**, 92 (2003).

[32] S. Pradhan, K. Samanta, K. Saha, and A. K. Nandy, Vector chirality kappa driven topological phase transition and the associated anomalous Hall conductivity tuning in a noncollinear antiferromagnet, arXiv:2206.15044.

[33] R. Shindou and N. Nagaosa, Orbital Ferromagnetism and Anomalous Hall Effect in Antiferromagnets on the Distorted fcc Lattice, Phys. Rev. Lett. **87**, 116801 (2001).

[34] C. Singh, V. Singh, G. Pradhan, V. Srihari, H. K. Poswal, R. Nath, A. K. Nandy, and A. K. Nayak, Pressure controlled trimerization for switching of anomalous Hall effect in triangular antiferromagnet Mn_3Sn, Phys. Rev. Res. **2**, 043366 (2020).

[35] N. Ito, T. Kikkawa, J. Barker, D. Hirobe, Y. Shiomi, and E. Saitoh, Spin seebeck effect in the layered ferromagnetic insulators $CrSiTe_3$ and $CrGeTe_3$, Phys. Rev. B **100**, 060402(R) (2019).

[36] Y. Liu and C. Petrovic, Three-dimensional magnetic critical behavior in CrI_3, Phys. Rev. B **97**, 014420 (2018).

[37] Y. Wang, C. Xian, J. Wang, B. Liu, L. Ling, L. Zhang, L. Cao, Z. Qu, and Y. Xiong, Anisotropic anomalous Hall effect in triangular itinerant ferromagnet Fe_3GeTe_2, Phys. Rev. B **96**, 134428 (2017).

[38] C. Tan, J. Lee, S.-G. Jung, T. Park, S. Albarakati, J. Partridge, M. R. Field, D. G. McCulloch, L. Wang, and C. Lee, Hard magnetic properties in nanoflake van der Waals Fe_3GeTe_2, Nat. Commun. **9**, 1554 (2018).

[39] A. F. May, D. Ovchinnikov, Q. Zheng, R. Hermann, S. Calder, B. Huang, Z. Fei, Y. Liu, X. Xu, and M. A. McGuire, Ferromagnetism near room temperature in the cleavable van der Waals crystal Fe_5GeTe_2, ACS Nano **13**, 4436 (2019).

[40] A. F. May, C. A. Bridges, and M. A. McGuire, Physical properties and thermal stability of $Fe_{5-x}GeTe_2$ single crystals, Phys. Rev. Mater. **3**, 104401 (2019).

[41] J. Seo, D. Y. Kim, E. S. An, K. Kim, G.-Y. Kim, S.-Y. Hwang, D. W. Kim, B. G. Jang, H. Kim, G. Eom, S. Y. Seo, R. Stania, M. Muntwiler, J. Lee, K. Watanabe, T. Taniguchi, Y. J. Jo, J. Lee, B. I. Min, M. H. Jo, H. W. Yeom, S.-Y. Choi, J. H. Shim, and J. S. Kim, Nearly room temperature ferromagnetism in a magnetic metal-rich van der Waals metal, Sci. Adv. **6**, eaay8912 (2020).

[42] S. Bera, S. K. Pradhan, R. Pal, B. Pal, A. Bera, S. Kalimuddin, M. Das, H. Afzal, A. N. Pal, and M. Mondal, Enhanced coercivity and emergent spin-cluster-glass state in 2D ferromagnetic material, Fe_3GeTe_2, J. Magn. Magn. Mater. **583**, 171052 (2023).

[43] Y. Liu, E. Stavitski, K. Attenkofer, and C. Petrovic, Anomalous Hall effect in the van der Waals bonded ferromagnet $Fe_{3-x}GeTe_2$, Phys. Rev. B **97**, 165415 (2018).

[44] S. Mondal, N. Khan, S. M. Mishra, B. Satpati, and P. Mandal, Critical behavior in the van der Waals itinerant ferromagnet Fe_4GeTe_2, Phys. Rev. B **104**, 094405 (2021).

[45] X. Yang, X. Zhou, W. Feng, and Y. Yao, Strong magneto-optical effect and anomalous transport in the two-dimensional van der waals magnets Fe_nGeTe_2 (n= 3, 4, 5), Phys. Rev. B **104**, 104427 (2021).

[46] Y. Gao, S. Yan, Q. Yin, H. Huang, Z. Li, Z. Zhu, J. Cai, B. Shen, H. Lei, Y. Zhang, and S. Wang, Manipulation of topological spin configuration via tailoring thickness in van der waals ferromagnetic $Fe_{5-x}GeTe_2$, Phys. Rev. B **105**, 014426 (2022).

[47] D. Rana, M. Bhakar, B. G., S. Bera, N. Saini, S. K. Pradhan, M. Mondal, and G. Sheet, High transport spin polarization in the van der Waals ferromagnet Fe_4GeTe_2, Phys. Rev. B **107**, 224422 (2023).

[48] J. Sau, S. R. Hassan, N. Kumar, and M. Kumar, Anomalous transport in itinerant van der Waals ferromagnets Fe_nGeTe_2 (n = 3, 4, 5), arXiv:2207.03547 [cond-mat.str-el].

[49] See Supplemental Material at http://link.aps.org/supplemental/10.1103/PhysRevB.108.115122 which includes experimental method, x-ray diffraction [64,65], Chemical characterization: EDX, Temperature-dependent anomalous Hall conductivity (σ_{xy}^{A}) [66], *ab initio* electronic structure calculations and Anomalous Hall Conductivity (AHC) simulations [67–75].

[50] S. Bera, S. K. Pradhan, M. S. Khan, R. Pal, B. Pal, S. Kalimuddin, A. Bera, B. Das, A. N. Pal, and M. Mondal, Unravelling the nature of spin reorientation transition in quasi-2d vdw magnetic material, Fe_4GeTe_2, J. Magn. Magn. Mater. **565**, 170257 (2023).

[51] R. Pal, B. Pal, S. Mondal, P. Mandal, and A. N. Pal, Unusual magnetotransport and anomalous Hall effect in

quasi-two-dimensional van der Waals ferromagnet Fe_4GeTe_2, arXiv:2303.07440.

[52] S. Roy, R. Singha, A. Ghosh, A. Pariari, and P. Mandal, Anomalous Hall effect in the half-metallic Heusler compound Co_2TiX (X = Si, Ge), Phys. Rev. B **102**, 085147 (2020).

[53] S. Chatterjee, J. Sau, S. Ghosh, S. Samanta, B. Ghosh, M. Kumar, and K. Mandal, Anomalous Hall effect in topological Weyl and nodal-line semimetal heusler compound Co_2VAl, J. Phys.: Condens. Matter **35**, 035601 (2023).

[54] P. Nozieres and C. Lewiner, A simple theory of the anomalous Hall effect in semiconductors, J. Phys. France **34**, 901 (1973).

[55] S. Onoda, N. Sugimoto, and N. Nagaosa, Intrinsic Versus Extrinsic Anomalous Hall Effect in Ferromagnets, Phys. Rev. Lett. **97**, 126602 (2006).

[56] T. Miyasato, N. Abe, T. Fujii, A. Asamitsu, S. Onoda, Y. Onoda, N. Nagaosa, and Y. Tokura, Crossover Behavior of the Anomalous Hall Effect and Anomalous Nernst Effect in Itinerant Ferromagnets, Phys. Rev. Lett. **99**, 086602 (2007).

[57] Q. Wang, S. Sun, X. Zhang, F. Pang, and H. Lei, Anomalous Hall effect in a ferromagnetic Fe_3Sn_2 single crystal with a geometrically frustrated Fe bilayer kagome lattice, Phys. Rev. B **94**, 075135 (2016).

[58] S. Chatterjee, J. Sau, S. Samanta, B. Ghosh, N. Kumar, M. Kumar, and K. Mandal, Nodal-line and triple point fermion induced anomalous Hall effect in the topological Heusler compound Co_2CrGa, Phys. Rev. B **107**, 125138 (2023).

[59] M. Lee, Y. Onose, Y. Tokura, and N. P. Ong, Hidden constant in the anomalous Hall effect of high-purity magnet MnSi, Phys. Rev. B **75**, 172403 (2007).

[60] S. Sangiao, L. Morellon, G. Simon, J. M. De Teresa, J. A. Pardo, J. Arbiol, and M. R. Ibarra, Anomalous Hall effect in Fe (001) epitaxial thin films over a wide range in conductivity, Phys. Rev. B **79**, 014431 (2009).

[61] C. Sürgers, G. Fischer, P. Winkel, and H. v. Löhneysen, Magnetotransport in ferromagnetic Mn_5Ge_3, $Mn_5Ge_3C_{0.8}$, and $Mn_5Si_3C_{0.8}$ thin films, Phys. Rev. B **90**, 104421 (2014).

[62] S. A. Baily and M. B. Salamon, Berry-phase contribution to the anomalous Hall effect in gadolinium, Phys. Rev. B **71**, 104407 (2005).

[63] Y. Onose and Y. Tokura, Doping dependence of the anomalous Hall effect in $La_{1-x}Sr_xCoO_3$, Phys. Rev. B **73**, 174421 (2006).

[64] A. F. May, M.-H. Du, V. R. Cooper, and M. A. McGuire, Tuning magnetic order in the van der Waals metal Fe_5GeTe_2 by cobalt substitution, Phys. Rev. Mater. **4**, 074008 (2020).

[65] M. Alghamdi, M. Lohmann, J. Li, P. R. Jothi, Q. Shao, M. Aldosary, T. Su, B. P. T. Fokwa, and J. Shi, Highly Efficient Spin-Orbit Torque and Switching of Layered Ferromagnet Fe_3GeTe_2, Nano Lett. **19**, 4400 (2019).

[66] D. F. Liu, A. J. Liang, E. K. Liu, Q. N. Xu, Y. W. Li, C. Chen, D. Pei, W. J. Shi, S. K. Mo, P. Dudin, T. Kim, C. Cacho, G. Li, Y. Sun, L. X. Yang, Z. K. Liu, S. S. P. Parkin, C. Felser, and Y. L. Chen, Magnetic Weyl semimetal phase in a Kagomé crystal, Science **365**, 1282 (2019).

[67] www.flapw.de.

[68] G. Kresse and D. Joubert, From ultrasoft pseudopotentials to the projector augmented-wave method, Phys. Rev. B **59**, 1758 (1999).

[69] J. P. Perdew, K. Burke, and M. Ernzerhof, Generalized Gradient Approximation Made Simple, Phys. Rev. Lett. **77**, 3865 (1996).

[70] J. P. Perdew and Y. Wang, Accurate and simple analytic representation of the electron-gas correlation energy, Phys. Rev. B **45**, 13244 (1992).

[71] H. J. Monkhorst and J. D. Pack, Special points for brillouin-zone integrations, Phys. Rev. B **13**, 5188 (1976).

[72] G. Pizzi, V. Vitale, R. Arita, S. Blügel, F. Freimuth, G. Géranton, M. Gibertini, D. Gresch, C. Johnson, T. Koretsune *et al.*, Wannier90 as a community code: new features and applications, J. Phys.: Condens. Matter **32**, 165902 (2020).

[73] N. Marzari and D. Vanderbilt, Maximally localized generalized wannier functions for composite energy bands, Phys. Rev. B **56**, 12847 (1997).

[74] Y. Yao, L. Kleinman, A. H. MacDonald, J. Sinova, T. Jungwirth, D.-s. Wang, E. Wang, and Q. Niu, First Principles Calculation of Anomalous Hall Conductivity in Ferromagnetic bcc Fe, Phys. Rev. Lett. **92**, 037204 (2004).

[75] Q. Wu, S. Zhang, H.-F. Song, M. Troyer, and A. A. Soluyanov, Wanniertools: An open-source software package for novel topological materials, Comput. Phys. Commun. **224**, 405 (2018).